Predicting the fatigue life of an AlSi10Mg alloy manufactured via laser powder bed fusion by using data from computed tomography

Yves Nadot, Carole Nadot-Martin, Wen Hao Kan, Sarah Boufadene, Matthew Foley, Julie Cairney, Gwénaëlle Proust, Lionel Ridosz

Version of Record: https://www.sciencedirect.com/science/article/pii/S2214860419302842
Manuscript_667e299186c8155a2d65c6ef403cc1b9

Predicting the fatigue life of an AlSi10Mg alloy manufactured via selective laser melting by using data from Computed Tomography

Yves Nadot[1], Carole Nadot-Martin[1], Wen Hao Kan[2,3], Sarah Boufadene[1], Matthew Foley[2], Julie Cairney[2,3], Gwénaëlle Proust[4], Lionel Ridosz[5]

[1] Institut Pprime, ISAE-ENSMA, Université de Poitiers, CNRS, 86961 Futuroscope cedex, France

[2] Australian Centre for Microscopy & Microanalysis, The University of Sydney, NSW 2006, Australia

[3] School of Aerospace, Mechanical and Mechatronic Engineering, The University of Sydney, NSW 2006, Australia

[4] School of Civil Engineering, The University of Sydney, NSW 2006, Australia

[5] SAFRAN Zodiac, Plaisir, France

Abstract

A modelling strategy is proposed to evaluate the influence of defect morphology on the fatigue limit of additively manufactured Al alloys by: (i) obtaining an x-ray micro-computed tomography (µ-CT) 3D image of the material, (ii) computing the Equivalent Inertia Ellipse of each individual pore, (iii) modelling the influence of the defect on the fatigue limit through the DSG approach and, (iv) 3D mapping the criticality of each individual defect.

For this fatigue study, an AlSi10Mg alloy was manufactured by selective laser melting using sub-optimal deposition parameters in order to produce large lack-of-fusion defects. After a T6 heat treatment, tension-compression fatigue tests, with R = -1, were conducted on specimens oriented with their loading axis either parallel or normal to the Z-axis of the additive manufacturing equipment. Two samples were characterised before µ-CT testing in order to characterise the initial 3D defect population. Each sample was fatigued step by step in order to determine the fatigue limit. The fracture surface was then carefully observed using a scanning electron microscope (SEM) in order to identify the critical defect in the initial µ-CT image. A comparison with the fatigue results led to the following conclusions: (i) when the longest axis of the defect is perpendicular to the load axis, modelling the defect as an equivalent inertia prolate ellipse gives better results (5 % error on the fatigue limit) than modelling it as a simple equivalent sphere (22 % error on the fatigue limit), (ii) the prolate ellipse is not relevant when the longest axis of the defect is oriented along the loading axis; in this case an oblate equivalent ellipse should be used, (iii) the concept of ‘size’ for a complex 3D shaped defect should be

linked to the inertia and the loading, (iv) with this approach, surface defects are shown to be more critical than internal ones for fatigue life and, (v) a 3D defect criticality map of the entire sample can be plotted to provide visual feedback on which defects are the most critical for fatigue life.

1. Introduction

Selective Laser Melting (SLM) is a specific additive manufacturing technique that utilises a high-powered laser to selectively melt and fuse metal powder particles that have been distributed across a powder bed, layer by layer, until the component being built is completed [1-3]. Compared to conventional manufacturing methods, SLM holds immense promise due to its ability to rapidly produce complex, near-net shaped components with far less material and energy wastage [3, 4]. The quality of a component built this way is, however, very sensitive to parameters such as the characteristics of the initial starting powder, the scan speed, the layer thickness, and the power of the laser [5]. Thus, SLM-fabricated alloys typically contain some amount of porosity, either due to the inability of the melted powder particles to flow into gaps (these pores are usually referred to as lack of fusion pores) or due to gases trapped within the melt pool (otherwise known as keyhole pores) [4]. Lack of fusion pores typically have irregular shapes and are often larger than keyhole pores, which are rather spherical.

Due to their excellent castability, mechanical properties, lightness and corrosion resistance, Al-Si alloys are of importance in the aerospace and automotive industries [1]. When Al-Si alloys are further alloyed with Mg and subjected to specific heat treatment processes, the precipitation of Mg_2Si can result in significant amounts of strengthening without detrimentally affecting other mechanical properties [1]. It is therefore not surprising that recently there has been considerable interest in applying and optimizing the SLM technique for the fabrication of AlSi10Mg components [1-5]. That being said, since fatigue life is crucial in aerospace and automotive industries for cost-effective design and safety [6], the presence of porosity in SLM-manufactured AlSi10Mg components can be a limiting factor to the use additive manufacturing for such applications.

While porosity plays a significant role in fatigue performance, other parameters such as the overall microstructure, residual stresses, and surface roughness/finish, of additive-

manufactured components should not be overlooked [2, 7-9]. In terms of the overall microstructure, in as-built AlSi10Mg alloys, crack propagation after the initiation of a fatigue crack tends to occur along melt pool boundaries [9]. Furthermore, since the Al grains of an as-built SLM-manufactured AlSi10Mg alloy are often columnar and oriented in the building direction, perpendicular to the border of a given melt pool, and since melt pool boundaries are directional [10, 11], it is not surprising that the mechanical properties, including fatigue life, of the alloy are also affected by anisotropy [8, 12]. One method of improving the fatigue life of as-built AlSi10Mg alloys is to simply alter the SLM parameters (such as hatch spacing and build orientation) to obtain an optimal microstructure [8]. It is also worth noting that the Al-grains in as-built AlSi10Mg alloys tend to contain a network of inter-dendritic cubic Si and extremely fine (nanoscale) Mg_2Si precipitates [10, 12]. Residual stresses in an SLM-fabricated material, on the other hand, are typically a result of thermal history such as the thermal gradient and cooling rate, and can be improved by altering the temperature conditions and/or the build height [12].

Since a subsequent T6 heat treatment applied to an as-built AlSi10Mg alloy will result in the dissolution of the melt pools, the diminution of residual stresses, and dissolution and precipitation of the inter-dendritic Si into a coarse globular morphology, a post heat-treated AlSi10Mg alloy typically displays good fatigue life [2, 9]. However, in both the as-built and heat-treated conditions, the porosity population, or more specifically, the presence of surface or sub-surface defects/porosity, will most likely still be the dominant factor that controls the fatigue properties of a given AlSi10Mg alloy [9, 13]. Therefore, there is a need to understand, model, and predict how the presence of such defects affect fatigue crack initiation and propagation in a given AlSi10Mg alloy.

The influence of surface/sub-surface pores on the fatigue life of SLM materials can be modeled using a variety of strategies. Beretta and Romano [14] proposed the approximation of sub-surface pores as pre-existing 2D cracks with a given depth, and a damage tolerance approach was used to propagate those cracks up to failure. A totally different approach suggested by Yang et al. [15] and Prithivirajan and Sangid [16] uses a non-local Fatigue Indicator Parameter (FIP) that takes into account the heterogeneity of local stresses. These non-local FIP approaches are similar to the Defect Size Gradient (DSG) criterion [17] that will be used for defect modelling in this particular study where the impact of a given defect is analyzed through a local stress gradient.

The objective of this paper is to study and model the effect of pore size, shape, orientation, and distance from the free surface on the High Cycle Fatigue (HCF) life of an SLM-fabricated AlSi10Mg alloy subjected to a T6 heat treatment. The 3D information of each pore present within the material will be obtained using µ-CT, and each individual pore will be modeled by approximating it as an Equivalent Inertia Ellipse (EIE). The DSG criterion will then be applied to each pore in order to assess and model its criticality. Finally, this model will be verified with experimental data. The model proposed in this study will allow the fatigue limit of an AlSi10Mg to be estimated assuming that the 3D information, including position relative to the surface, of all pores in the alloy is known. This will allow a 3D defect size map criticality of the entire material to be plotted that provides visual feedback on which defects are the most critical.

Material and experimental details

Specimens were fabricated using an Additive Layer Manufacturing process using laser powder bed technology with a pre-alloyed powder (average particle size of 32 µm). The layering is performed by means of a scraper with a layer thickness of 50 µm. The powders have a chemical composition in accordance with the DIN EN 1706:2010 standard (weight %: Si 9-11 / Fe < 0.55 / Mg 0.2-0.45 / Mn < 0.45 / Zn < 0.1 / T < 0.15). Standard parameters used are as follows: production temperature 150 °C, hatch distance 170 µm, Power 350 W, speed 930 mm/s. In order to release the stresses induced by the process, a one-hour post-processing heat treatment was performed at 210 °C. Finally, a T6 heat treatment was performed on the material before machining: 540 °C for 8 h / water quench to 20 °C / natural aging at 20 °C for 24 h / artificial aging at 160°C for 10 h / natural cooling down to 20°C. Deliberately sub-optimal operating parameters were used in order to produce large, oriented defects that are representative of an optimal process, but on a larger scale. The largest defects are therefore lack of fusion pores that are highly oriented and can be easily characterized by µ-CT. 90 x 90 x 20 mm blocks were built and fatigue samples (Figure 1ab) were machined out of these blocks by using electric discharge machining. The loading axis of the fatigue samples are perpendicular (referred to as XY) or parallel (referred to as Z) to the building direction. Fatigue samples were tested in the as-machined condition without polishing with an average roughness R_a close to 1 µm.

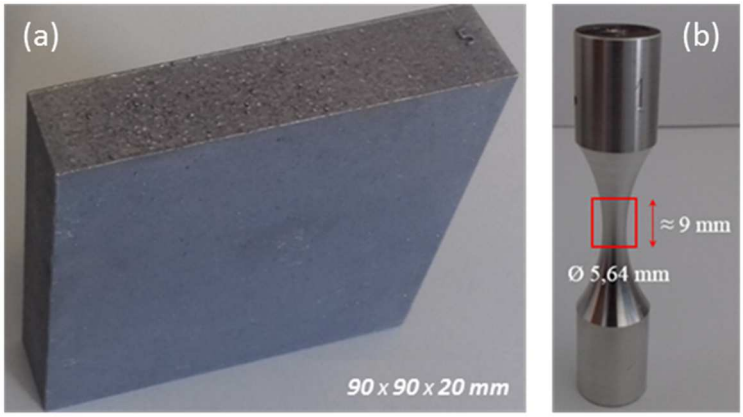

Figure 1: (a) Raw material (b) Fatigue sample.

The microstructure of the material has been characterized before and after T6 treatment. Figure 2 shows a 3D summary of the results. The organization of the melt pools is presented on Figure 2a where the trace of the laser can be clearly observed. After T6 (Figure 2b) the melt pools disappeared (as observed on Figure 2a) and the Si reorganized into coarse precipitates that are homogeneously distributed over space. Crystallographic grains (Figure 2c) are generally not modified by the T6 treatment and they remain strongly oriented/textured, from a geometrical viewpoint, along the z axis. As a result, the 'grain size' in the XY plane is about 10 times smaller than in the XZ or YZ planes. A '3D size' of the grains should be used rather that a unique size parameter to analyze grains from the morphological viewpoint.

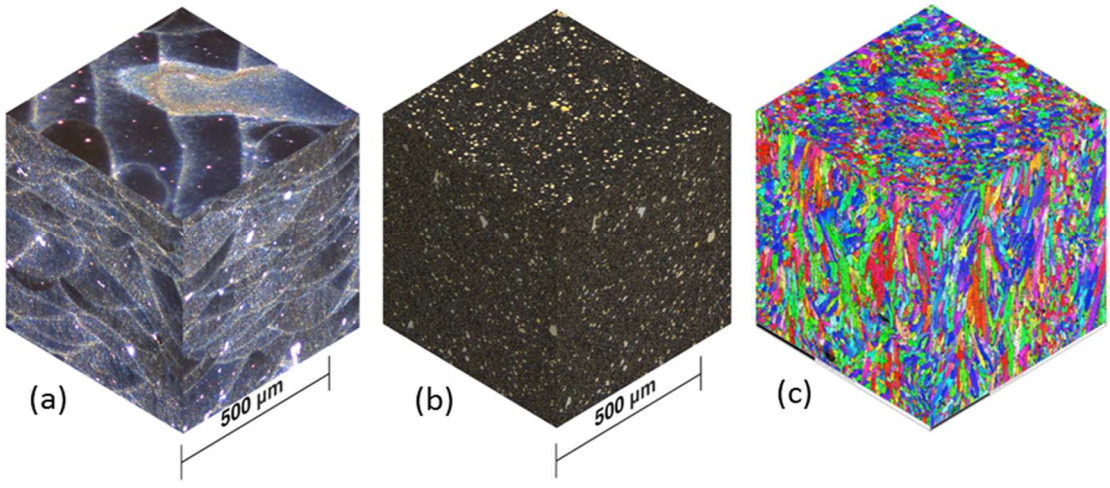

Figure 2: building direction: vertical - same scale on all images - cube 600 µm x 600 µm x 600 µm, (a) microstructure before T6 (dark field optical image), (b) microstructure after T6 (dark field optical image), (c) electron backscatter diffraction (EBSD) inverse pole figure (IPF) map of the Al grains after T6.

The porosity of the material was imaged in 3D using µ-CT with an Xradia MicroXCT-400 system operating at a beam energy of 60 kVp / 166 µA. Specimens were positioned relative to the source and detector such that a pixel resolution of 4.7 µm could be obtained. A total of 3000 projections was collected with 10 s exposures. Reconstruction was performed using XMReconstructor 7.0.2817, with all reconstruction parameters kept constant to produce axial image stacks with isotropic voxel dimensions. The collected data was then analysed using Avizo, a 3D image analysis software. The defect population was obtained on samples Z1 and XY16. Figure 3 shows the sphericity of the defect population relative to the size of the corresponding defects, with a sphericity of 1 representing a perfect sphere and the defect size defined as the diameter of an equivalent sphere by volume. The defect population distribution across both samples is slightly different due to the heterogeneous distribution of defects across the original built material. As most defects smaller than 100 µm in diameter correspond to keyhole defects inherited from the laser/material interaction at the tip of the melt pool, it makes sense that they tend to be spherical in size. Defects larger than 100 µm in size, on the other hand, are far from spherical and can be associated with a lack of fusion during the process. It is important to remark that, while there are very few large defects, these defects tend to be the most critical for fatigue life, and therefore, the average defect size of the entire defect population can be very misleading. Instead, any analysis of the defect size must also consider the distribution of defect sizes. Furthermore, the density of the material, while strongly linked to the average defect size, is not the relevant parameter for fatigue analysis as fatigue failure is mainly governed by the largest defect.

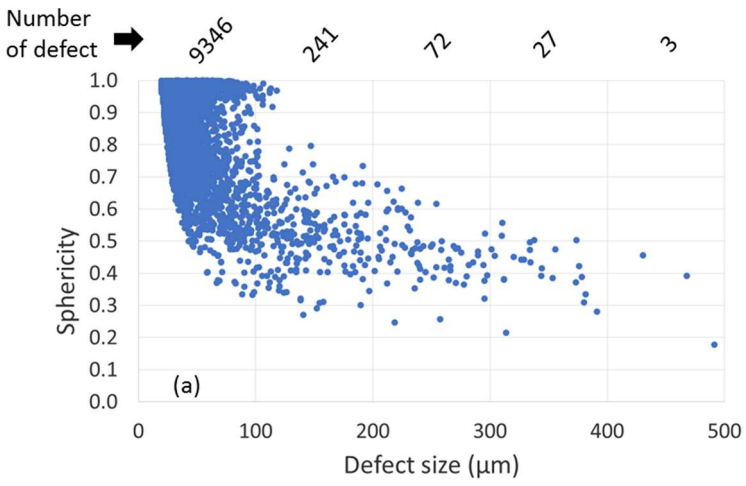

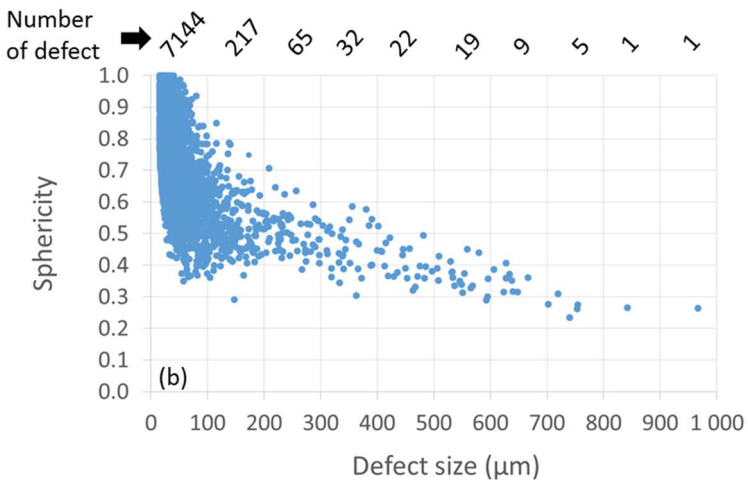

Figure 3: Defect population and sphericity for (a) sample Z1 (b) sample XY16.

In order to define the orientation of defects over space, two angles are used, as shown on Figure 4a, to characterise the orientation of the longest axis of the EIE. The angle Φ, characterising the long axis of the ellipse compared to the Z direction, is plotted on Figures 4b and c as a function of defect size for defects larger than 100 µm. It is shown that the long axes of the ellipsoids representing the defects are strongly perpendicular to the Z axis (i.e. the loading direction) in the case of the Z samples, which means that all large defects are lack of fusion defects that were formed in the planes where the layering process happens. The XY sample shows a random distribution of the angle Φ, revealing that there are no specific orientations for large defects relative to the loading direction for these specimens.

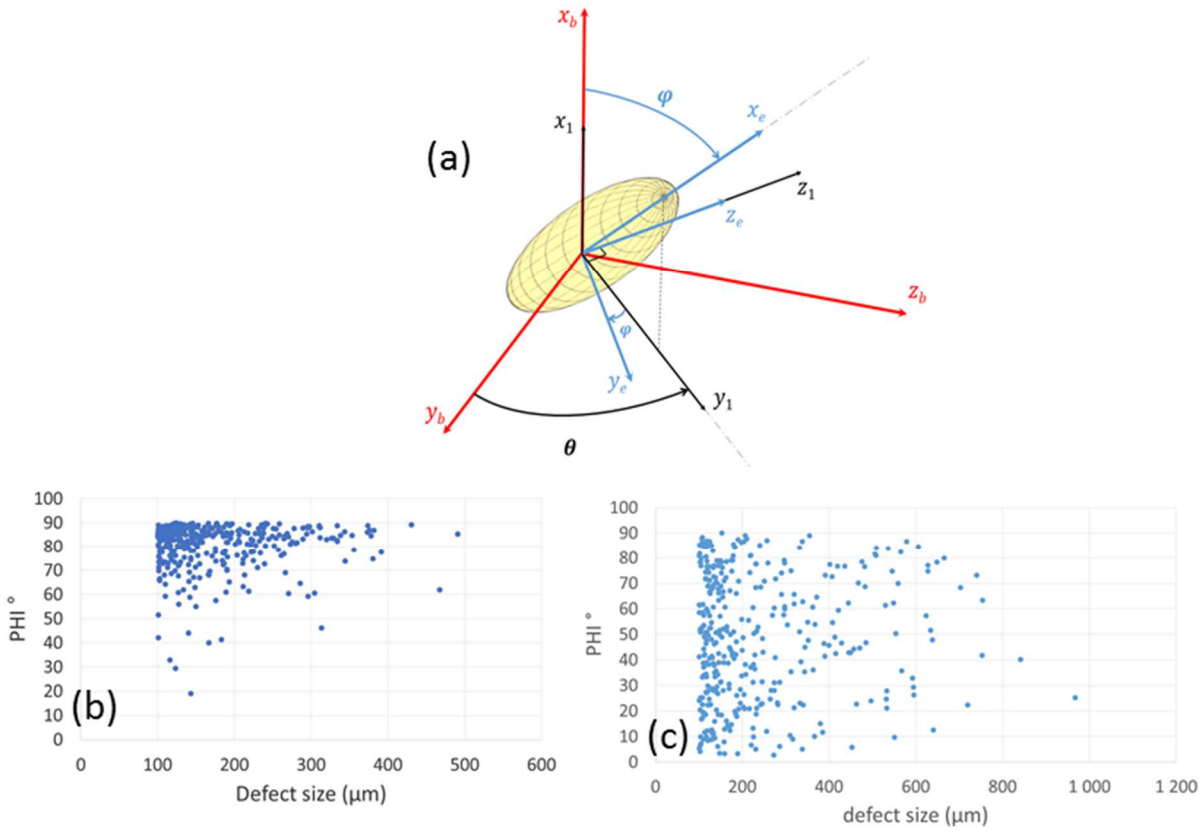

Figure 4: (a) axis systems: (x_b; y_b; z_b) is the sample global axis system with x_b corresponding to the building direction; (x_e; y_e; z_e) is the local ellipsoid (representing the defect) axis system, (b) and (c) show the orientation of the axis of maximum principal inertia (x_e), φ, as a function of defect size for sample Z1 and sample XY16 respectively.

From the µ-CT images, it is possible to show a 3D view of the 50 largest defects (the number was arbitrarily chosen for ease of visualisation). As it will be explained in the modelling section, surface defects and internal defects must be distinguished. The surface and internal defect definition used here are based on previous work [18, 19]. Surface defects are defined as 'open porosity' in terms of the 3D µ-CT images and can be said to be directly in contact with ambient air. That being said, there are some "closed pores", however, that are sufficiently close to the surface such that the ligament distance to the surface from such a defect is smaller than its size. Since this can lead to a rapid failure of the ligament, such defects should also be considered as surface defects even if they are not initially exposed to ambient conditions. It, therefore, follows that a defect is defined as internal when its size is smaller than the ligament length to the surface [18].

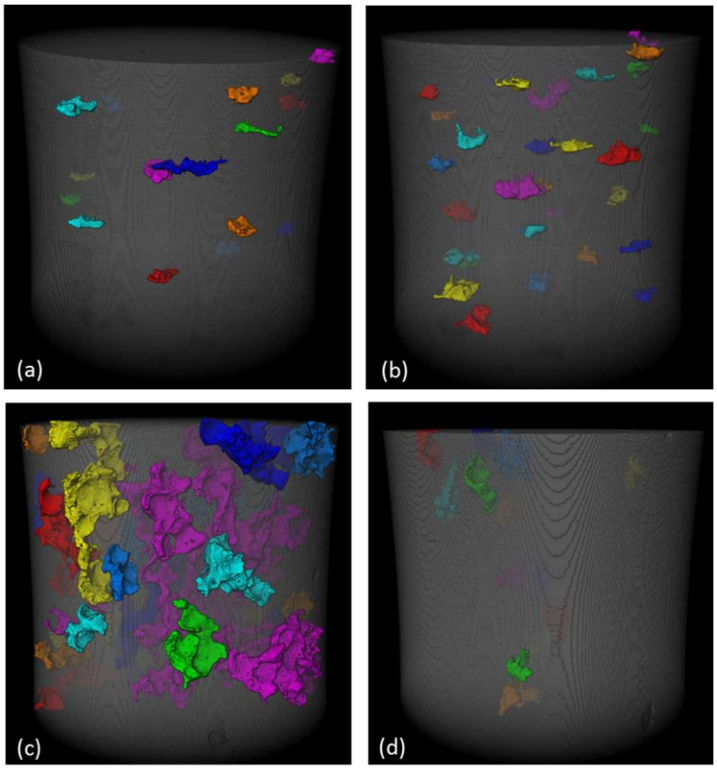

Figure 5: 50 biggest defects selected for visualization, with the colors added to aid in identifying individual defects: (a) sample Z1 surface defects, (b) sample Z1 internal defects (c) sample XY16 surface defects and, (d) sample XY16 internal defects.

Fatigue results

Fatigue tests were conducted on a hydraulic INSTRON loading frame under force-controlled conditions. The tensile fatigue load was applied with a load ratio of R = -1 at a frequency of 20 Hz with a sinusoidal wave signal. The end of a test is defined as the total failure of the sample. During the test, force and displacement were recorded in order to verify load changes across the total number of fatigue cycles. Tests were conducted in the High Cycle Fatigue (HCF) regime, far below the known yield strength of the material, with fatigue lives ranging from 40,000 to 1,000,000 cycles. From Figure 6, it can be concluded that the average behavior of both sample sets (XY and Z) is very similar in the whole range of fatigue life tested for this material. Naturally, the results will be analyzed through fracture surface observations and the quantification of defect size, shape and orientation. It is relatively surprising that the Z samples did not perform worse than the XY samples since it was initially expected that the large lack of fusion defects should be detrimental to the fatigue life of the Z samples as these defects are strongly oriented perpendicularly to the loading axis (i.e. parallel to the crack propagation

plane). A recent study from Domfang [20] showed that in the T6 condition and for a material containing defects smaller than 60 µm, Z samples tend to display better fatigue behavior compared to XY samples, which is contrary to the findings here. However, it is important to keep in mind that the analysis of the defect population showed that the maximum defect size is not the same for all the samples due to the inhomogeneity generated by the manufacturing process itself, which could explain the previous result.

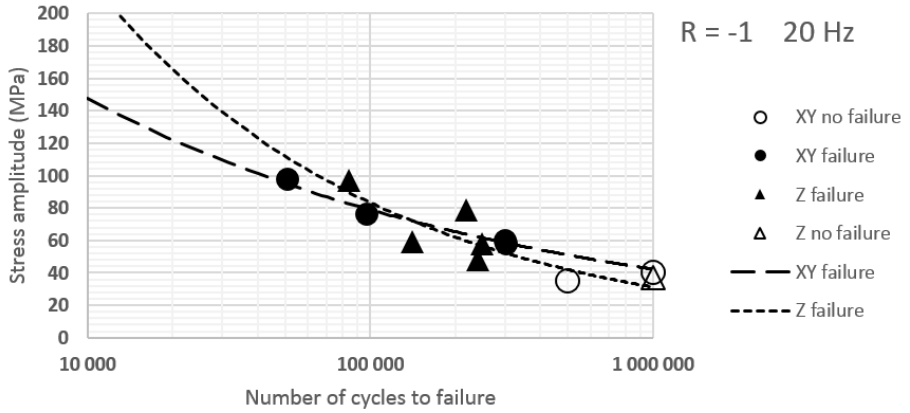

Figure 6: fatigue tests results under tension-compression, 20 Hz, R = -1.

Two fracture surfaces for each condition are presented in Figure 7. In these SEM images difference in defect orientation between the XY and Z samples is very clear. The defects generally look like ‘flakes’ distributed over space. The presence of numerous defects on a given fracture surfaces is due to the crack plane propagating through these defects rather than these defects being crack initiation sites. Therefore, the critical defect(s) responsible for crack initiation must be identified. This can be done by tracing all the “river-like” marks on the fracture surface until they converge to a unique defect. The Z samples (shown in Figures 7 a and b) generally reveal relatively clean fracture surfaces with unique crack initiation sites (white arrow) and a few other defects along the propagation plane. XY samples tend to be much more difficult to analyze because of the number of defects and the difficulties in identifying the “river-marks” to find the initiation site locations. This may indicate multiple initiation sites for a single test sample, as observed on sample XY12 (Figure 7d). The size of the critical defect is measured on the fracture surface using the Murakami’s parameter [21], with the results presented directly on Figure 7

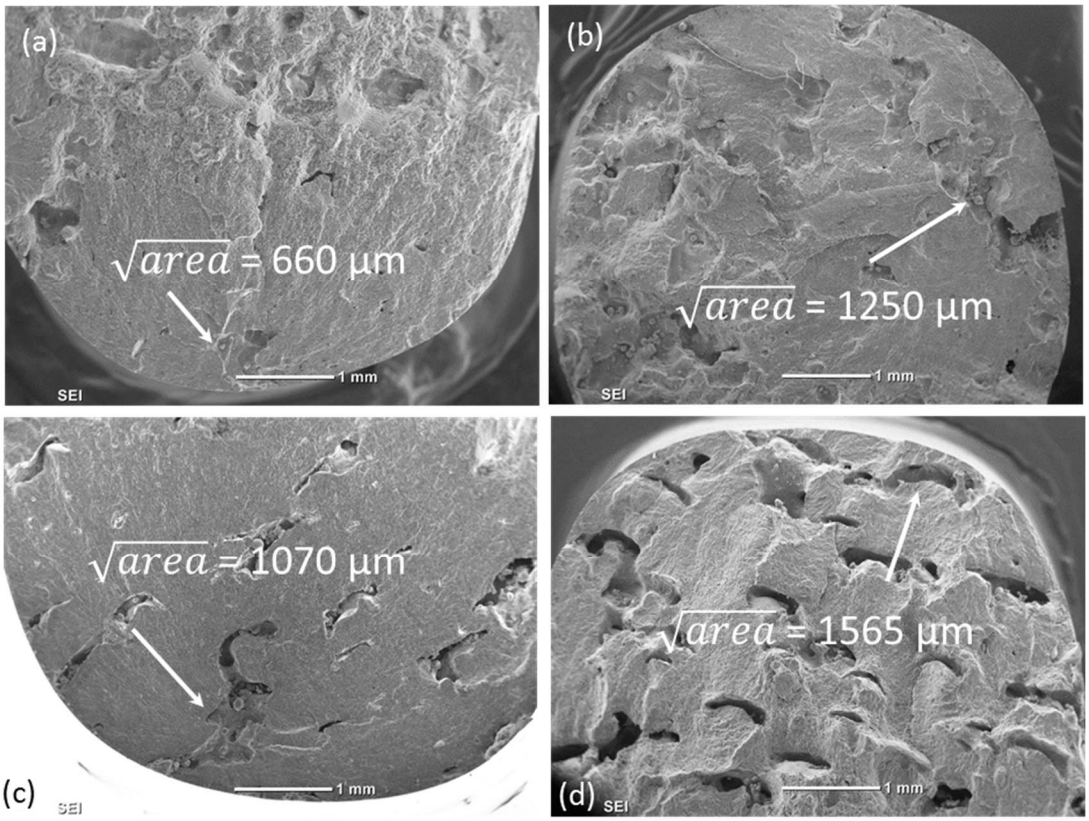

Figure 7: Secondary electron images of fracture surfaces obtained using a SEM, critical defect highlighted by the white arrow (a) Sample Z4 (σ = 79 MPa; N_R = 219,000) (b) Sample Z6 (σ = 59 MPa; N_R = 141,000) (c) Sample XY15 (σ = 56 MPa; N_R = 310,000) (d) Sample XY12 (σ = 76 MPa; N_R = 97,000).

Finally, two samples were prepared in order to validate the whole modeling strategy: Z1 and XY16 (µ-CT images shown previously in Figure 5) were loaded step by step (1 million cycles per step) up to failure in order to get and estimation of the fatigue limit. Results are presented on Figure 8. For both samples, the fatigue limits are similar despite the strong difference in size and morphology of the critical defect identified on each fracture surface. These results are consistent with the previous fatigue tests performed on XY and Z samples. Each defect is carefully observed and measured in order to identify it in the µ-CT scan.

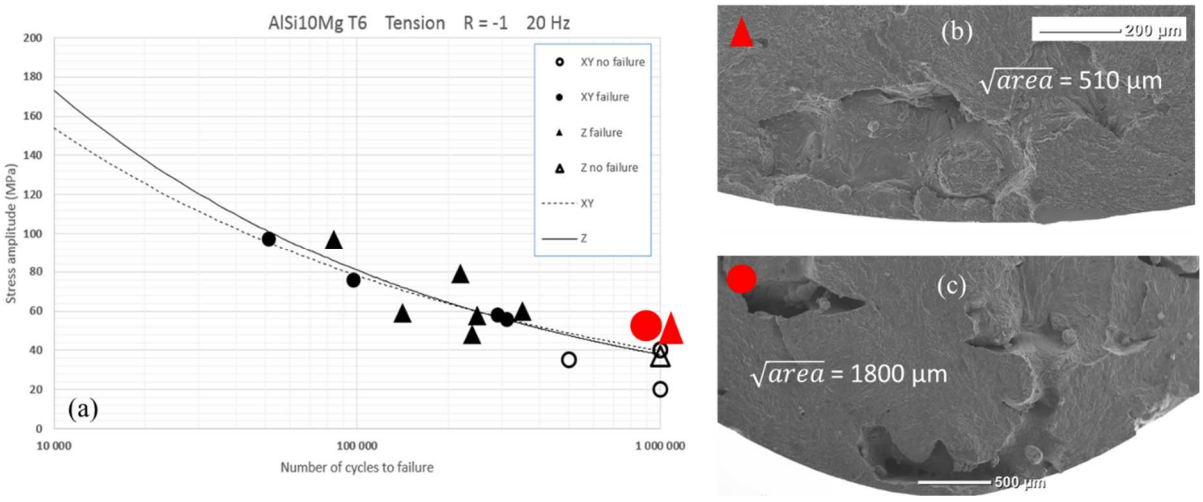

Figure 8: Step by step fatigue test on samples previously observed by µ-CT (a) Fatigue test results (b) Fracture surface for sample Z1 (c) Fracture surface for sample XY16.

Modeling the impact of defects on fatigue limit

From the experimental results, we can conclude that the fatigue life is strongly influenced by the presence of defects. It seems that the influence is not the same depending on the fatigue life: a longer fatigue life typically corresponds to a single crack initiation site while a short fatigue life tends to correspond to multiple initiation sites. This conclusion is relevant to the fatigue of metals under primarily tensile loading and is also promoted here by the fact that the defect population is dense, with the defects being relatively large and close to one another. In the following section we will focus on HCF (fatigue lives close to one million cycles) where we will consider that the governing mechanism is initiation of a single crack from an isolated defect.

This section covers the hypothesis, the criterion, the identification procedure, the application of the criterion to µ-CT scan and finally a comparison with the experimental results.

The modeling strategy aims at evaluating the impact of defects on the fatigue limit. The following assumptions are made:

- The fatigue limit is defined as the stress amplitude for one million cycles.
- Crack initiation is assumed to be the principal mechanism governing the fatigue limit.
- The material's behavior remains fully elastic at the macroscopic scale.
- Defects do not modify the macroscopic behavior.

- Each defect is considered isolated with no interaction with other defects.
- Each individual defect is characterized by its center of gravity, its volume, its global shape and its inertia matrix. The equivalent size and shape will be discussed for each defect.
- Stress computation at the local scale on the periphery of a given defect does not take plasticity into account.

In order to account for the influence of each defect on the fatigue limit, the Defect Stress Gradient (DSG) criterion is used. This criterion describes the impact of the defect through the local stress gradient that the defect creates at the local scale. The DSG criterion describes the effect of morphology [22, 23], multi-axial loading, including load ratio effect [24], and has been improved with the analytical Eshelby theory [17] that allows the criterion to be applied as a post treatment of a Finite Element (FE) computation of complex parts in order to plot defect size maps [25]. The criterion has been tested on several materials: cast Ti64, cast A345T6, cast A357T6, nodular cast iron, cast Inconel 718, 1045 steel, and ARMCO iron, and has shown good results when the identification procedure carefully accounts for the defect type. The following explains the basics of the concept but it is recommended that the reader refer to the aforementioned references for more details.

The DSG criterion describes the impact of a given defect through the stress gradient of the equivalent fatigue stress over the defect size. The criterion can be computed using different definitions of the equivalent stress in accordance with material and loading considered. Equation (1) presents the criterion.

$$\sigma_{DSG} = \sigma_{cr\mathrm{M}} - a_{\nabla} \nabla\sigma_{cr\mathrm{M}} \quad ; \quad \nabla\sigma_{cr\mathrm{M}} = \frac{\sigma_{cr\mathrm{M}} - \sigma_{cr0}}{size} \tag{1}$$

Next, the Crossland [26] fatigue criterion is used because the multi-axial loading addressed is proportional. The Crossland stress is given by Equation (2)

$$\sigma_{\mathrm{cr}} = \sqrt{J_{2a}} + \alpha_{cr}\, \sigma_{Hmax} \tag{2}$$

where $\sqrt{J_{2a}}$ is the second invariant of the amplitude of the deviatoric stress tensor, σ_{Hmax} the maximum hydrostatic stress over a cycle, and α_{CR} a material parameter. Thus, $\sigma_{cr\mathrm{M}}$ in Equation (1) is the maximum value over the defect surface of the Crossland stress and σ_{cr0} its value far from the defect. The latter corresponds to the equivalent stress that would exist if the material was free of defect. The a_{∇} parameter describes the influence of the defect through the stress gradient. The DSG approach does not depend on the criterion so another scalar equivalent fatigue stress could be used.

Finally, the DSG 'stress' (Equation (1)) is compared to a scalar that represents the fatigue limit of the material without defect for the considered fatigue stress (Equation (3))

$$\sigma_{DSG} < \beta_{cr} \tag{3}$$

If this inequality is true then no failure by fatigue can occur.

The DSG criterion summarized in equations (1-3) can be applied at each point of space with respect to the hypothesis mentioned and can therefore be applied to the samples for which µ-CT images are available.

The DSG criterion needs the maximum local Crossland stress at the surface of the defect to be evaluated in order to compute the stress gradient. In the present paper, the real 3D complex defect will be represented by a prolate ellipse with an equivalent inertia matrix. In order to compute the local stresses around the defect, the Eshelby theory is used. The theory is detailed in [17] for both spheroidal and ellipsoidal inclusions. The Eshelby theory is an analytical theory giving the local stress and strain field inside and outside the inclusion, the material (matrix) surrounding the inclusion being linear elastic. In our case, the inclusion will be a void. In order to get the maximum value of the Crossland stress at the surface of the defect, a discretization of the ellipse is proposed. The discretization over space is a function of the shape factor considered and 2594 points are used in order to have a good representation of the variation of stresses at the surface of the ellipse. As observed in Figure 9, the number of points is higher closer to the extremity of the ellipsoid. With such a discretization, it is possible to capture the maximum local von Mises stress within a 2 % error. The comparison was also made with the Crossland equivalent stress with the same error. We will use the computation from the analytical Eshelby theory in the next section.

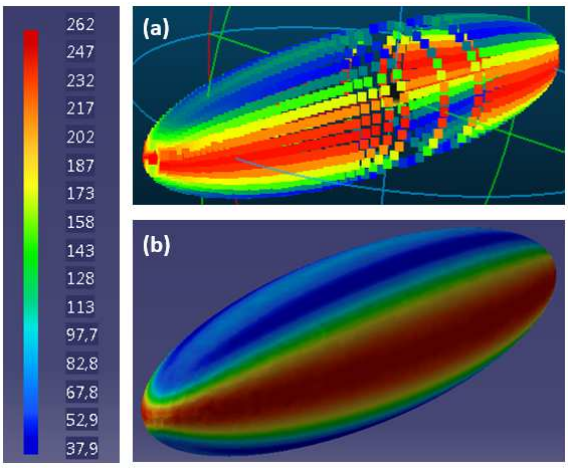

Figure 9: Comparison of the von Mises stress distribution at the same scale, for an elliptical defect with a shape factor of 4 and a vertical loading of 100 MPa: (a) Eshelby analytical computation, 3D rendering (b) Finite Element computation.

Identification procedure

The criterion presented in Equations 1-3 requires the identification of three material parameters. α_{CR} and β_{CR} are identified using two different fatigue limits without defects. These two parameters describe the multi-axial behavior of the material without defects. As the experimental results of the present study do not allow for the fatigue limit of a material without defects to be obtained, experimental results from Beretta [14] are used. Beratta compiled several results from the literature on AlSi alloys manufactured by SLM process and after T6 treatment. With the results plotted as a Kitagawa-type diagram, it is possible to estimate the fatigue limit for a 'defect free' material. The fatigue limits obtained are, for R = -1 and R = 0.1, 100 and 75 MPa respectively. The identification of the a_{∇} parameter requires a fatigue limit for a given known defect. Fatigue tests have been conducted on another batch of material (same machine, same powder) that contains rather 'spherical' porosities. The fatigue limit obtained is 76 MPa for a spherical defect size of 250 µm as measured on the fracture surface.

In order to take into account the position of a given defect, as suggested by Serrano et al. [27], a different set of parameters will be used for surface and internal defects. Serrano observed an increase in the stress amplitude resulting in fatigue failure for a given fatigue life (cast AlSi material) of 20 % for the base material without defects under vacuum. We will consider that this 20 % increase can be applied to SLM AlSi materials so that the β_{CR} parameter is 95 MPa under vacuum. We will assume that the α_{CR} parameter describing the influence of mean stress

and the a_∇ parameter that describes the influence of the defect are not modified by the position of the defect.

The three material parameters of the DSG criterion can be calculated and Table 1 presents a summary of the material data needed and the values of the parameters for both surface and internal defects.

Table 1: *experimental results used for the identification of the DSG criterion and values of the parameters. Nomenclature* $\sigma_{D-1}^{ten}(360\ \mu m)$*:* σ_D *= fatigue limit (stress amplitude at 1 million cycles), ten = tension, -1 = load ratio, (360* μm*) = defect size.*

Experimental results	**Material parameter Surface defect (AlSi SLM T6)**	**Material parameter Internal defect (AlSi SLM T6)**
$\boldsymbol{\sigma_{D-1}^{ten}(no\ defect) = 100\ MPa}$ [14] $\boldsymbol{\sigma_{D0,1}^{ten}(no\ defect) = 75\ MPa}$ [14]	$\alpha_{CR} = 0.64$	$\alpha_{CR} = 0.64$
$\boldsymbol{\sigma_{D-1}^{ten}(\text{sphere } 250\ \mu m) = 76\ MPa}$ Hypothesis: 20% increase of fatigue limit under vacuum [27]	$\beta_{CRsurf} = 79\ MPa$	$\beta_{CRint} = 95\ MPa$
	$a_\nabla = 173\ \mu m$	$a_\nabla = 173\ \mu m$

Validation of the modelling strategy

For each set of defects analyzed on Figure 5, each individual defect was characterized by its volume, its equivalent diameter and two angles describing the orientation of the long axis of the inertia matrix of the defect. The general methodology is presented in Figure 10. The gauge lengths of the Z and XY fatigue samples investigated for this modeling study were first subjected to 3D µ-CT scans prior to fatigue testing. The scanned data was then analyzed using Avizo 9.3 where each individual defect was isolated and measured so that the EIE can be calculated for each defect. The analysis of the main inertia direction allows the two angles related to each defect's orientation over space to be obtained for the longest axis of the ellipsoid, with the orientation of each defect measured in relation to the loading axis. The DSG criterion was then computed for each defect (with different sets of parameters depending on the position of the defect) and a 3D image was drawn to illustrate the computed criticality of each individual defect. Finally, the results from the simulation were then compared to the

experimental results in order to determine if the critical defect calculated using this model is indeed the critical defect that led to fatigue failure. This general methodology takes into account the following five major defect parameters: type, size, position, morphology and orientation relative to loading. It should also be stated that the accuracy of Avizo in conducting the aforementioned measurements was prior validated by using Avizo to analyze several 3D pure ellipsoids of varying orientations and shape ratios that were drawn using the CAD software Catia. The results between the two software were shown to be in good agreement.

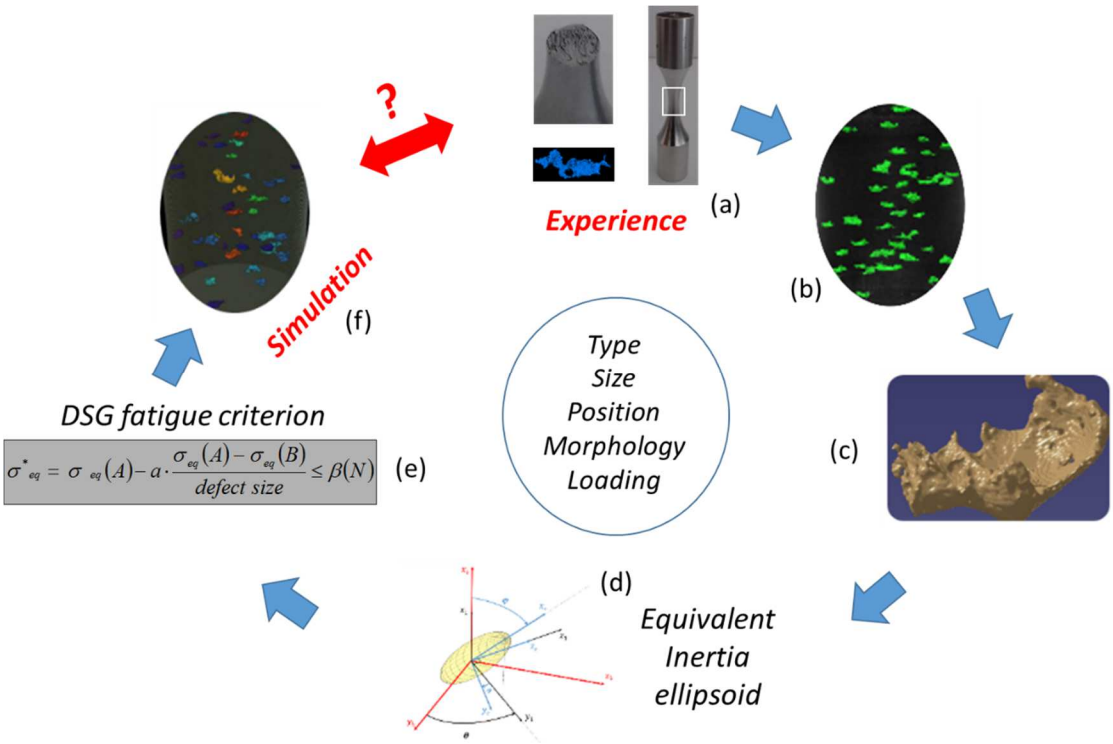

Figure 10: Modelling strategy: (a) fatigue sample: fatigue limit and critical defect identified, (b) 3D µ-CT image of the gauge section, (c) each porosity is imaged in 3D and labeled, (d) the EIE is computed, (e) the DSG criterion is computed for each individual defect, (f) 3D rendering of the criticality of all defects.

Table 2 shows the modeling results obtained for all surface defects of sample Z1. The applied stress is the experimental fatigue limit of the sample, the size of the defect is defined as its equivalent diameter, the shape factor is evaluated from the inertia matrix (see equation 4), the angle Φ is the orientation of the defect relative to the loading axis (see Figure 4) and 'error DSG' is the error obtained when comparing experimental results to the DSG stress (see Equation 5).

$$shape\ factor = \sqrt{\frac{2\ I_2}{I_1}} \qquad (4); \qquad Error\ DSG = \frac{\sigma_{DSG} - \beta_{Cr}}{\beta_{Cr}} * 100 \qquad (5)$$

A positive value for error DSG means that the defect will initiate a crack because the value of the DSG stress exceeds that of β_{cr} that represents the experimental fatigue limit. When the value of the error DSG is negative, the defect will not initiate a crack. Therefore, a perfect simulation of a single critical defect that would initiate a crack leading to fatigue failure should result in a 0 % error, and all other (non-critical) defects, surface or internal, should result in a negative error value. The simulation results shown in Table 2 also consider the impact of modeling each defect as a sphere or a prolate ellipsoid. In the case of the former, the angle φ is irrelevant (since a sphere does not have an orientation) while angle φ is important for the latter.

Table 2 shows that the representation of each defect as a sphere gives very conservative results since none of the defects will initiate a crack, which is not exactly the case since the sample was found to reach its fatigue limit experimentally. It can also be noticed that the error is directly proportional to the defect size for a sphere so the biggest defect is the most critical. When the defects are represented using the EIE, the results are significantly more consistent with the experimental results. While the errors for all the defects are still negative, the four most critical defects had errors lower than -5 % (i.e. very close to the ideal 0 %). By analyzing the fracture surface, the actual critical defect can be determined. Based on its morphology and position from the surface (see Figure 11), this defect was identified in the 3D µ-CT dataset as defect "33" (highlighted in Table 2). Interestingly, this defect was found to have the highest shape factor but not the biggest size. The error DSG is very close to 0 for this defect so from a modeling perspective, this defect is highly likely to initiate a crack. Defects number 28, 1 and 30 could also be considered as critical from the modeling perspective even though they did not initiate the fatal crack.

Table 2: results of the DSG model for each surface defect (among the biggest), sample Z1

defect number	size µm	shape factor	Φ °	Error DSG Sphere %	Error DSG Ellipsoid %
28	371	2.5	86	- 18	- 3
1	396	2.0	88	- 16	- 3
30	364	2.3	84	- 18	- 5
33	310	4.5	88	- 23	- 5
42	331	2.4	90	- 21	- 8
43	326	2.2	88	- 21	- 9
36	328	2.1	72	- 21	- 12
16	314	1.9	88	- 22	- 13
9	329	2.2	61	- 21	- 15
50	300	1.9	82	- 24	- 15
22	273	2.8	84	- 27	- 15
38	263	3.5	87	- 28	- 16
47	275	2.4	88	- 27	- 16
13	269	2.9	80	- 27	- 17
24	285	2.0	79	- 25	- 17
21	257	2.4	78	- 29	- 21

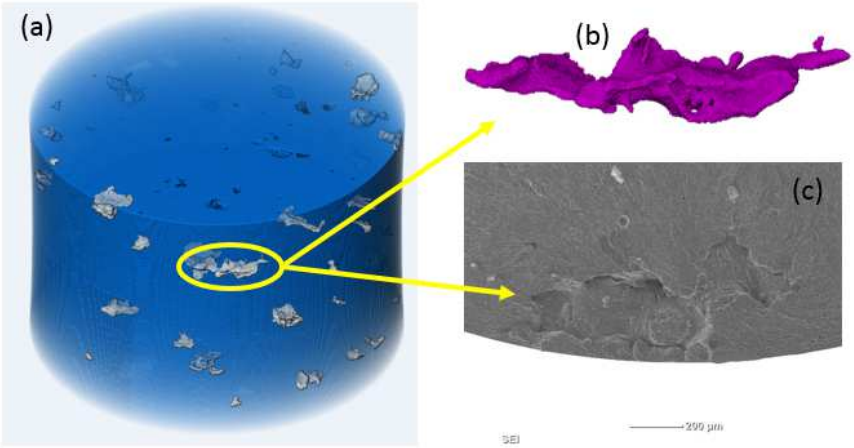

Figure 11: Sample Z1, fatigue limit = 53 MPa: (a) 3D view of the biggest surface porosities, (b) 3D view of the critical defect number 33, (c) critical defect number 33 as observed on the fracture surface after the test.

Finally, it is therefore possible to plot a 3D criticality map (Figure 12) where each defect is assigned a color based on its error DSG, which in this case, is represented by black or dark

blue. This illustrative approach can be a very powerful tool in helping engineers determine the quality (in terms of fatigue performance) of a given additively manufactured part.

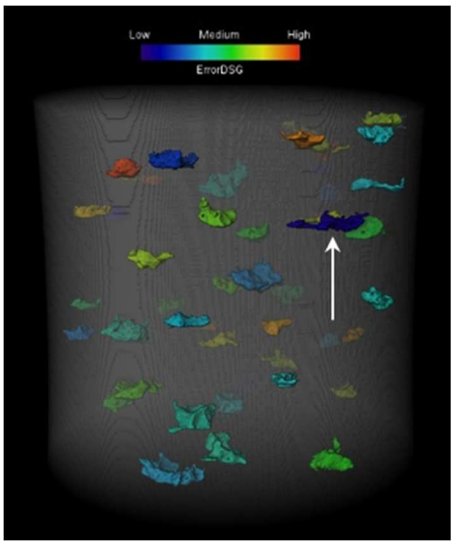

Figure 12: sample Z1, defect size map criticality: minimum error = most critical defect, dark blue, defect number 33 indicated by white arrow.

The table for internal defects is not presented because it does not bring fundamentally new results. The error DSG for the set of internal defects range from -26 to -37 % when the defect is represented by a sphere and -13 to -29 % when the defect is represented by the EIE. All internal defects are considered as non-critical even though they may be larger than any of the surface defects. For instance, one of the largest internal defects (specifically defect number 37) has a size of 495 µm and a shape factor of 2.36 but only an error DSG of -18 %. This is because the fatigue limit for a defect free material under vacuum is higher than for surface initiation under ambient air. Of course, considering the fact that the internal defects are under vacuum could be erroneous because it is not demonstrated. Residual gases, specifically Ar, can be present in the porosities since Ar was used as a shielding gas during the additive manufacturing process. Ideally, fatigue tests should be conducted under an Ar environment to quantify the impact of this environment on the fatigue limit.

Sample XY16 was then tested and analyzed using the same modelling strategy. Figure 13 presents the critical defect from the µ-CT image and the associated fracture surface. The 3D view presents only the critical defect because, as shown in Figure 5, a set of very large defects is present in the gauge section of this sample. It can be observed that the defect shape is extremely complex and the size observed on the fracture surface was very large (1800 µm, as

illustrated on Figure 8c). With this sample, we are facing a morphology that is very far from being representable by a sphere or an ellipsoid. The size parameter, which is very important in this model, is very difficult to define since there is no simple geometry that this defect can be modeled upon. Furthermore, it is difficult to obtain a reasonable measurement of the defect size or the crack initiation site from the fracture surface image alone. Nevertheless, we will apply the same simulation model to this sample in order to evaluate the limits of this methodology for very complex shape defects.

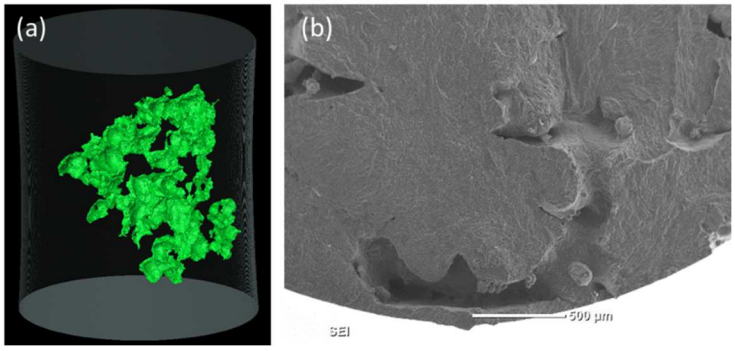

Figure 13: Sample XY16, fatigue limit = 45 MPa (a) 3D view of the critical defect (b) fracture surface showing the critical defect.

Results presented on Table 3 reveal that eight of the defects are considered to be critical and could initiate a crack (positive % 'errorDSG ellipsoid'). These defects are among the largest though there are non-critical defects that may be larger since the DSG criterion depends not just on defect size, but also the shape ratio and orientation. Defect number 22, the actual critical defect that led to failure during the experimental fatigue test, is the 3rd most critical defect from the error DSG computation so while the quantitative value was not correctly estimated from the model, the qualitative evaluation compared to all other defects is relatively accurate (even more so than the sample Z1 computation). When the defects are represented using a sphere in the model ('errorDSG sphere'), the absolute errors are lower as compared to the ellipsoidal model but all defects are now considered non-critical. It seems that in the case of extremely complex defect morphology, the spherical model may lead to better results. Nevertheless, we can't draw quantitative conclusions from this complex shape defect sample containing extremely large defects. A prolate ellipsoid is an oriented equivalent defect in only one direction and with the 'flake' oriented along the load axis, the angles Φ are randomly distributed so that a 'unique' direction as per the model of the prolate is not relevant. Another

model should be introduced to represent this defect: the oblate ellipse. In this case, the geometry would be correctly described.

Table 3: results of the DSG model for each surface defect (among the biggest), sample XY16.

defect number	size µm	shape factor	Φ °	errorDSG sphere %	ErrorDSG %	ellipsoid
2	876	3.9	86	-8	20	
12	1040	3.6	73	-7	18	
22	879	3.2	80	-8	16	
50	687	3.5	88	-11	14	
23	893	2.4	71	-8	8	
1	665	2.5	80	-12	7	
43	505	2.7	84	-16	2	
3	531	2.1	88	-15	0	
4	445	2.6	78	-18	-3	
48	484	2.4	70	-17	-4	
9	381	3.1	89	-22	-4	
42	409	2.4	88	-20	-5	
34	421	2.9	68	-19	-6	
26	410	2.3	80	-20	-7	
21	628	2.4	53	-12	-8	
41	467	3.0	54	-17	-11	
37	565	4.3	45	-14	-12	
47	468	2.4	52	-17	-14	
36	499	2.2	44	-16	-18	
32	439	2.4	47	-19	-18	
25	918	3.2	30	-8	-22	
11	1670	2.0	22	-4	-23	
18	464	2.3	38	-17	-23	
17	666	2.3	30	-12	-24	
6	925	2.0	19	-8	-27	
40	380	5.4	32	-22	-30	
31	894	2.3	17	-8	-30	
28	571	2.2	13	-14	-34	
24	424	2.3	20	-19	-34	
16	572	2.2	9	-14	-35	
46	440	3.2	18	-19	-37	
33	479	2.4	10	-17	-37	
20	950	3.9	12	-8	-39	
39	398	2.4	11	-21	-39	
5	797	4.2	4	-9	-43	

Finally, it should also be stated that as additive manufacturing matures, it is possible that lack of fusion defects can be substantially minimized. If the defects that remain are small spherical gas porosities, the spherical model may be more appropriate.

Conclusion

The following conclusions can be drawn from fatigue tests conducted under tension-compression fatigue tests with R = -1 on ALM AlSi10Mg T6 material produced under deliberately sub-optimal process parameters (high number of lack of fusion oriented defects).

- The material contains a large amount of lack of fusion porosities. The porosity rate is very important, varying from 1 to 6 % depending on the sample. Defect size goes up to more than 1000 µm and the shape is strongly oriented perpendicularly to the building direction.
- The T6 heat treatment annihilates the initial melt pool organization to create a homogeneously distributed structure of Si precipitates. The anisotropy of grain shape associated with initial melt pools is not modified by the T6.
- In order to account for environmental effect, the defect population of the gauge section of fatigue sample is separated into three categories: internal, sub-surface and surface. Internal defects are considered being under vacuum whereas sub-surface and surface ones are under air environment. Fatigue parameter identification is different for internal and surface defects.
- A modeling strategy is proposed based on the DSG multiaxial criterion coupled to an evaluation of the stress field at the defect surface by the Eshelby theory. Each individual defect is modeled with an Equivalent Inertia Ellipsoid, a local stress gradient is computed including size effect and the criticality of each defect can be plotted.

Comparison with experimental results shows that:

- Modeling the defect using a prolate ellipsoid is a good starting point to capture morphology effect but still limited description for the defect observed in the material. An oblate ellipsoid will be also considered for a better description of all different shapes.
- The use of the multiaxial fatigue criterion methodology should be limited to fatigue lives higher than 1 million cycles. Below this value, the crack propagation is probably important in the whole fatigue life.

Acknowledgements

The authors gratefully acknowledges funding provided by Zodiac Aerospace. The authors acknowledge the facilities, and the scientific and technical assistance, of the Microscopy Australia (formerly the Australian Centre for Microscopy and Microanalysis Research Facility) at The University of Sydney and Centre for Advanced Structural Engineering (CASE) at the University of Sydney

References

[1] K. Kempen, L. Thijs, J. Van Humbeeck, J.P. Kruth, Mechanical Properties of AlSi10Mg Produced by Selective Laser Melting, Physics Procedia 39 (2012) 439-446.

[2] E. Brandl, U. Heckenberger, V. Holzinger, D. Buchbinder, Additive manufactured AlSi10Mg samples using Selective Laser Melting (SLM): Microstructure, high cycle fatigue, and fracture behavior, Materials & Design 34 (2012) 159-169.

[3] C. Weingarten, D. Buchbinder, N. Pirch, W. Meiners, K. Wissenbach, R. Poprawe, Formation and reduction of hydrogen porosity during selective laser melting of AlSi10Mg, Journal of Materials Processing Technology 221 (2015) 112-120.

[4] N.T. Aboulkhair, N.M. Everitt, I. Ashcroft, C. Tuck, Reducing porosity in AlSi10Mg parts processed by selective laser melting, Additive Manufacturing 1-4 (2014) 77-86.

[5] N. Read, W. Wang, K. Essa, M.M. Attallah, Selective laser melting of AlSi10Mg alloy: Process optimisation and mechanical properties development, Materials & Design (1980-2015) 65 (2015) 417-424.

[6] Y. Gao, J. Yi, P. Lee, T. Lindley, The effect of porosity on the fatigue life of cast aluminium-silicon alloys, Fatigue & Fracture of Engineering Materials & Structures 27(7) (2004) 559-570.

[7] T. DebRoy, H. Wei, J. Zuback, T. Mukherjee, J. Elmer, J. Milewski, A. Beese, A. Wilson-Heid, A. De, W. Zhang, Additive manufacturing of metallic components–process, structure and properties, Progress in Materials Science (2017).

[8] M. Tang, P.C. Pistorius, Oxides, porosity and fatigue performance of AlSi10Mg parts produced by selective laser melting, International Journal of Fatigue 94 (2017) 192-201.

[9] N.T. Aboulkhair, I. Maskery, C. Tuck, I. Ashcroft, N.M. Everitt, Improving the fatigue behaviour of a selectively laser melted aluminium alloy: Influence of heat treatment and surface quality, Materials & Design 104 (2016) 174-182.

[10] L. Thijs, K. Kempen, J.-P. Kruth, J. Van Humbeeck, Fine-structured aluminium products with controllable texture by selective laser melting of pre-alloyed AlSi10Mg powder, Acta Materialia 61(5) (2013) 1809-1819.
[11] J. Wu, X.Q. Wang, W. Wang, M.M. Attallah, M.H. Loretto, Microstructure and strength of selectively laser melted AlSi10Mg, Acta Materialia 117 (2016) 311-320.
[12] A.H. Maamoun, M. Elbestawi, G.K. Dosbaeva, S.C. Veldhuis, Thermal post-processing of AlSi10Mg parts produced by Selective Laser Melting using recycled powder, Additive Manufacturing 21 (2018) 234-247.
[13] J. Damon, S. Dietrich, F. Vollert, J. Gibmeier, V. Schulze, Process dependent porosity and the influence of shot peening on porosity morphology regarding selective laser melted AlSi10Mg parts, Additive Manufacturing 20 (2018) 77-89.
[14] S. Beretta, S. Romano, A comparison of fatigue strength sensitivity to defects for materials manufactured by AM or traditional processes, International Journal of Fatigue 94 (2017) 178-191.
[15] K.V. Yang, P. Rometsch, T. Jarvis, J. Rao, S. Cao, C. Davies, X. Wu, Porosity formation mechanisms and fatigue response in Al-Si-Mg alloys made by selective laser melting, Materials Science and Engineering: A 712 (2018) 166-174.
[16] V. Prithivirajan, M.D. Sangid, The role of defects and critical pore size analysis in the fatigue response of additively manufactured IN718 via crystal plasticity, Materials & Design 150 (2018) 139-153.
[17] M. Vincent, C. Nadot-Martin, Y. Nadot, A. Dragon, Fatigue from defect under multiaxial loading: Defect Stress Gradient (DSG) approach using ellipsoidal Equivalent Inclusion Method, International journal of fatigue 59 (2014) 176-187.
[18] M. Iben Houria, Y. Nadot, R. Fathallah, M.J. Roy, D. M. Maijer, Influence of casting defect and SDAS on the multiaxial fatigue behaviour of A356-T6 alloy including mean stress effect, International Journal of Fatigue, Volume 80, pp. 90-102, 2015
[19] A. Rotella, Y. Nadot, M. Piellard, R. Augustin , M. Fleuriot, Fatigue limit of a cast Al-Si-Mg alloy (A357-T6) with natural casting shrinkages using ASTM standard X-Ray inspection, International Journal of Fatigue 114 (2018), 177-188
[20] J. N. Domfang Ngnekou, Y. Nadot, G. Henaff, J Nicolai, W. H. Kan, J. M. Cairney, L. Ridosz, Fatigue properties of AlSi10Mg produced by Additive Layer Manufacturing, 119 (2019) 160–172
[21] Murakami Y, Effects of small defects and nonmetallic inclusions. 1st ed.Amsterdam: Elsevier; 2002

[22] T. Billaudeau, Y. Nadot and G. Bézine, Fatigue limit for defective materials: mechanisms and experiments, Acta Materiala, 52, 3911-3920, 2004
[23] Y. Nadot and T. Billaudeau, Multiaxial fatigue limit criterion for defective materials, Eng Fract Mech (73), 1, pp. 112-133, 2006
[24] H. Gadouini, Y. Nadot and C. Rebours, Influence of mean stress on the multiaxial fatigue behaviour of defective materials, Int J of Fatigue , 30 (9) pp. 1623-1633, 2008
[25] A. Rotella, Y. Nadot, R. Augustin, M. Piellard, S. L'Heritier, Defect size map for cast A357-T6 component under multiaxial fatigue loading using the Defect Stress Gradient (DSG) criterion, Engineering Fracture Mechanics, 174 (2017) 227–242
[26] B. Crossland, Effect of large hydrostatic pressures on the torsional fatigue strength of fan alloy steel. In: Proc. int. conf. fatigue met.; 1956. p. 138–49
[27] I. Serrano-Munoz, J.-Y. Buffiere, R. Mokso, C. Verdu et Y. Nadot, Location, location & size: defects close to surfaces dominate fatigue crack initiation, Scientific report, 2017, 7:45239